ADVANCED
ENERGY & SUSTAINABILITY
RESEARCH
Open Access
www.advenergysustres.com

Localized Surface Plasmon Resonance and Field Alignment Boosted Photocatalytic H_2O_2 Production of ZnO/Au–CN through Configuration Design

Rongke Sun, Jiaqi Liu, Xue Yu, Yanmei Ren, Huawei Zhao, Hongyuan Zhao, Yanqing Ma, and Lei Ma**

Highly aligned ZnO nanoarrays are designed that exhibit dual catalytic and thermoelectric properties. By integrating C_3N_4 nanosheets onto the ZnO nanoarrays, a vertical ZnO–C_3N_4 (ZnO–CN) thermoelectric catalytic heterojunction is constructed. The alignment of thermoelectric potential along the ZnO nanorods largely enhances the intensity of the built-in electric field within the heterojunction. Additionally, by introducing Au nanoparticles (Au NPs) on the top of ZnO nanoarrays, thermoelectric performance is further elevated due to a 2.8-fold increase in temperature gradient induced by localized surface plasmon resonance effect. Experimentally, the ZnO/Au-CN demonstrates a photocatalytic H_2O_2 production rate of 43.79 mmol h^{-1} m^{-2} with 2 °C cooling water. Herein, an avenue in the design of novel thermoelectric catalytic systems is provided.

1. Introduction

Hydrogen peroxide (H_2O_2) is a versatile and environmentally friendly oxidant that has been widely utilized in pollutant purification, medical disinfection, and industrial bleaching.[1–4] However, conventional methods for H_2O_2 production are expensive both in monetary cost and energy consumption since the heavy usage of precious metals and hydrogen gas.[5,6] Photocatalytic reduction of oxygen to H_2O_2 with sunlight presents a promising solution to mitigate both energy requirement and environmental pollution.[3,7–9] However, the high recombination rate of charge carriers severely limits the performance of photocatalysts.[10,11] Hence, it is crucial to construct structures that can effectively promote the separation of photogenerated electrons and holes and maintain high oxidation and reduction capabilities simultaneously.[12,13]

The intrinsic driving force for charge carrier separation in heterojunctions is the electric field, which facilitates the directional migration of photogenerated carriers.[14–17] The field is the result of surface polarization resulted by the uneven charge distribution at the heterojunction interface.[18] However, the built-in electric field typically extends only a few nanometers at the interface that leads to a rapid recombination of photogenerated charge carriers away from the space charge region due to the abrupt decay of driving force.[19,20] Consequently, it is essential to develop a catalytic system that can maintain high intensity of built-in electric field over a large distance.

By harnessing environmental heat, thermoelectric catalytic system offers a leeway to directly build an electric field in heterojunction photocatalysts.[21–24] In such kind of systems, the light irritated on the catalyst surface acts as heat sources to generate thermoelectric fields.[25,26] Adding up the intrinsic built-in electric field, the intensity and spatial range of the overall electric field in the heterojunction can be significantly extended. This positive synergistic effect could highly improve both the catalytic efficiency and photothermal stability of the thermoelectric catalyst.[27] The integration of thermoelectric effects with catalysis was first explored in the 1970s by T. Otagawa and his colleagues through combining commercial thermoelectric devices with photoelectrocatalytic systems. By effectively converting solar energy to heat through Fresnel lenses, they achieved a thermoelectric potential of 2 V and supplied to the catalytic electrodes, which largely reduced the reliance on external energy input.[28] However, advances confront the contemporary limit of nanofabrication technology, particularly in meeting the design requirements of highly integrated catalytic systems.[27] Consequently, research has shifted toward integrating low-dimensional thermoelectric materials, such

---

R. Sun, J. Liu, X. Yu, Y. Ren, H. Zhao, H. Zhao, Y. Ma, L. Ma
Tianjin International Center for Nanoparticles and Nanosystems
Tianjin University
No. 92 Weijin Road, Tianjin 30072, P. R. China
E-mail: mayanqing@tju.edu.cn; lei.ma@tju.edu.cn

Y. Ma, L. Ma
Tianjin Key Laboratory of Low-dimensional Electronic Materials and Advanced Instrumentation
No. 92 Weijin Road, Tianjin 30072, P. R. China

Y. Ma
School of Precision Instrument and Opto-electronics Engineering, Tianjin University
No. 92 Weijin Road, Tianjin 30072, P. R. China

Y. Ma, L. Ma
Haihe Laboratory for Low-dimensional Electronic Materials
Add 1 to No. 57, Wujiayao Street, Tianjin 30074, P. R. China

The ORCID identification number(s) for the author(s) of this article can be found under https://doi.org/10.1002/aesr.202500120.

DOI: 10.1002/aesr.202500120

as nanoparticles,[29,30] nanorods,[31] and nanosheets[32,33] with catalysts. Benefiting from intrinsic electronic structure of the composite system, temperature gradients of it can lead to thermoelectric fields under illumination, further enhancing their catalytic performance. However, the random orientation of thermoelectric fields could lead to mutual cancellation and further diminishing the catalytic performance enhancement. Therefore, it is crucial to develop strategies that can effectively increase the temperature gradient and align the thermoelectric field in thermoelectric catalyst systems.

ZnO–C_3N_4 is a well-established heterojunction photocatalytic system; moreover, ZnO also exhibits excellent thermoelectric properties.[34,35] By rationally designing ZnO structures, their inherent thermoelectric effects could be harnessed to significantly boost the catalytic performance. In this work, we designed a highly aligned ZnO nanoarrays that exhibit dual catalytic and thermoelectric catalysis enhancement. By integrating C_3N_4 nanosheets onto the ZnO nanoarrays, a vertical ZnO–CN thermoelectric catalytic heterojunction was formed. The aligned thermoelectric field along the ZnO nanorods strengthens the intensity of the built-in electric field within the heterojunction under illumination. Additionally, the introduction of Au NPs on the top of ZnO nanoarrays further elevates their thermoelectric performance compared to the bare ZnO–CN, due to a 2.8-fold increasement in temperature gradient induced by LSPR effect. Through a self-built temperature-variable photocatalytic reaction cell, the ZnO/Au–CN demonstrates a photocatalytic H_2O_2 production rate of 43.79 mmol h^{-1} m^{-2}. A systematic investigation on the relationship between the temperature gradient and catalytic performance provides new insights into the mechanisms of thermoelectric catalytic enhancement.

2. Results and Discussion

Figure 1a illustrates the synthesis procedure of C_3N_4 nanosheets via a thermal polycondensation process. As shown in Figure 1b,

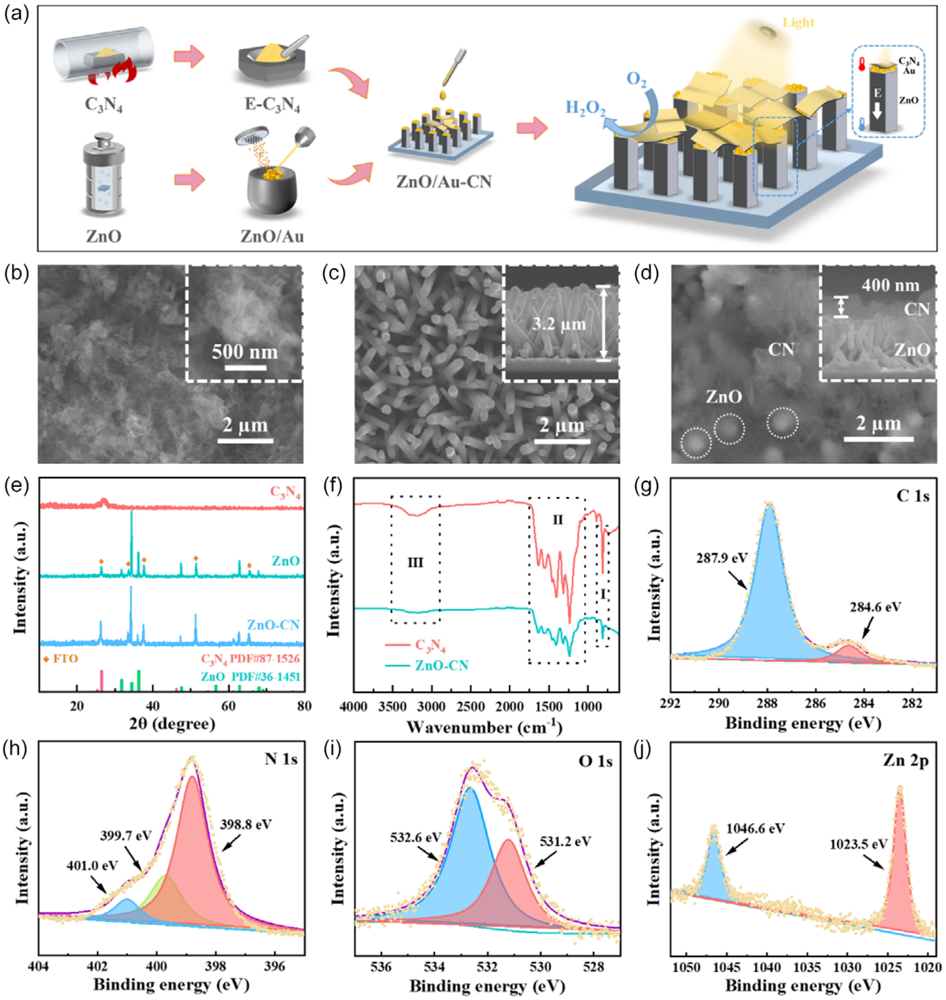

Figure 1. a) Schematic diagram of ZnO/Au–CN preparation. SEM images of b) C_3N_4, c) ZnO, and d) ZnO–CN. The inset illustrations of (b,c, and d) show the SEM images of C_3N_4 with high magnification, crossview SEM image of ZnO nanoarrays, and crossview SEM image of ZnO-CN, respectively. e) XRD spectra of C_3N_4, ZnO, and ZnO–CN. f) FTIR spectra of C_3N_4 and ZnO–CN. XPS spectra of g) C 1s and h) N 1s of C_3N_4. XPS spectra of i) O 1s and j) Zn 2p of ZnO.

the material exhibits a flocculent structure, and the inset high-magnification image reveals the gauze-like appearance of the nanosheets. Figure 1c shows the morphology of ZnO nanoarrays synthesized by a hydrothermal method, where the nanorods grow quasivertically on the surface of the FTO substrate with a height of ≈3.2 μm. Further statistical analysis reveals that the average diameter of the ZnO nanorods is 258.9 nm (Figure S1, Supporting Information). Figure 1d shows the morphology of ZnO–CN, where the gauze-like C_3N_4 nanosheets are uniformly loaded on top of the ZnO nanoarrays. The underlying ZnO nanoarrays are barely visible beneath the thin C_3N_4 layer. The inset crossview scanning electron microscope (SEM) image indicates that the thickness of the C_3N_4 layer is ≈400 nm. Due to the large surface area and 2D gauze-like structure of C_3N_4, it is uniformly distributed on the top of the ZnO, rather than being embedded within the gaps of the nanoarrays. The energy dispersive spectroscopy (EDS)s exhibit distinct peaks corresponding to C, N, O, and Zn, further confirming the effective decoration of C_3N_4 on the ZnO nanoarrays (Figure S2, Supporting Information). The structures of the synthesized materials were characterized by X-ray diffraction (XRD). As shown in Figure 1e, the upper red line represents the XRD pattern of C_3N_4, which exhibits two distinct diffraction peaks at 21.6 and 26.5°, well matching with the powder diffraction file (PDF) card (PDF#87-1526) for C_3N_4. These two peaks are attributed to the (100) and (002) crystal planes of the hexagonal C_3N_4 *P*-6m2 unit cell.[14] The middle green line is the XRD pattern of the synthesized ZnO nanoarrays, which exhibits clear diffraction peaks corresponding to both ZnO and the fluorine-doped tin oxide (FTO) substrate. The ZnO displays a typical hexagonal wurtzite structure with three prominent peaks at 34.42, 36.25, and 62.86° that correspond to the (002), (101), and (103) planes of the ZnO P63mc unit cell (PDF#36-1451), respectively.[36] Notably, this material demonstrates a significant preferential growth along the (002) plane indicating strong anisotropy in the ZnO nanoarrays. This dominant orientation is beneficial to the uniform thermoelectric potential output.[37] The blue line represents the XRD pattern of the ZnO–CN. Due to the weak crystallization and low loading of C_3N_4, no distinct diffraction peaks of C_3N_4 are observed. Additionally, the diffraction peaks of the composite remain nearly identical to those of pure ZnO that indicates a minute distortion in the crystal structure of ZnO due to the incorporation of C_3N_4. Figure 1f presents the fourier transform infrared spectroscopy (FTIR) spectra of C_3N_4, which exhibit characteristic absorption peaks in three regions (I, II, and III). The peak at 810 cm^{-1} corresponds to the characteristic vibration mode of the triazine ring in C_3N_4. The peaks at 1253, 1320, and 1425 cm^{-1} are attributed to the stretching vibrations of the aromatic C—N bonds in C_3N_4. The peaks at 1572 and 1632 cm^{-1} correspond to the in-plane stretching vibrations of the C═N bonds. The broad peak in the 3000–3750 cm^{-1} range is caused by the stretching vibrations of N—H bonds.[38–40] These results verify the successful synthesis of the C_3N_4. The FTIR spectrum of the ZnO–CN shows no significant changes in the position or number of the characteristic absorption peaks compared to pure C_3N_4, with only a slight decrease in absorption intensity. This indicates that the formation of the composite does not alter the structure of the C_3N_4. The chemical compositions of the prepared materials were characterized using XPS. Figure 1g displays the C 1s spectrum of the C_3N_4, where two distinct peaks at 287.9 and 284.6 eV are observed. The peak with higher binding energy corresponds to sp^2-hybridized carbon (C—N═C) in C_3N_4, while the peak with lower binding energy is attributed to adsorbed carbon from the environment. Figure 1h presents the N 1s spectrum of C_3N_4 with peaks located at 401.0, 399.7, and 398.8 eV corresponding to N—H_x, N—C_3, and C═N—C, respectively.[41,42] Figure 1i shows the O 1s spectrum of the ZnO nanoarrays, where the peak at 531.2 eV is assigned to lattice oxygen in Zn—O, and the peak at a slightly higher binding energy is attributed to the surface-adsorbed oxygen and hydroxyl groups. In Figure 1j, the Zn 2p spectrum exhibits two characteristic peaks at 1046.6 and 1023.5 eV, referring to Zn $2p_{1/2}$ and Zn $2p_{3/2}$, respectively.[11,43] These results collectively confirm the successful synthesis of the C_3N_4, ZnO, and ZnO–CN.

Figure 2a presents the light absorption efficiency of C_3N_4 and ZnO. It reveals the strong absorption of ZnO in the ultraviolet region with the absorption edge at ≈386 nm. In contrast, the synthesized C_3N_4 shows a much stronger light absorption capacity in the visible range with the absorption edge around 455 nm. As shown in Figure 2b, the calculated optical bandgap of C_3N_4 is ≈2.57 eV, while that of ZnO is around 3.19 eV. The flat band potentials of the materials were characterized through electrochemical MS measurements. As presented in Figure 2c,d, the positive slopes of the MS curves for C_3N_4 and ZnO indicate that both materials exhibit n-type semiconductor feature, denoting the closeness of flat band potential to the conduction band edge[44] which can be used as an approximation for the conduction band position.[45–47] Based on the results from multiple frequency tests, the flat band potential of C_3N_4 is approximately −0.5 V, while that of ZnO is around −0.19 V, both values are higher than the reduction potential of O_2 to H_2O_2 (0.08 V vs. NHE).[42] The work functions of C_3N_4 and ZnO were further characterized using kelyin probe force microscopy (KPFM) to determine the Fermi level positions. Figure 2e shows the surface morphology of the sample, where C_3N_4 is loaded on the surface of the ZnO nanoarrays with a clear interface. Figure 2f displays the work function mapping obtained from the same scan area, where a clear difference in the work functions of the two materials can be observed. As shown in Figure 2g,h, the thickness of C_3N_4 is ≈500 nm, and the work function of C_3N_4 is lower than that of ZnO, about 150 mV. The above test results are summarized in Figure 2i, indicating that during the formation of the heterostructure, electrons will spontaneously transfer from C_3N_4 to ZnO due to the potential difference. Finally, it leads to the equalization of the Fermi levels of the two materials and the formation of a built-in electric field at the interface aligned from C_3N_4 to ZnO (Figure 2j).[12] Under the exertion of this built-in electric field, the photogenerated holes in C_3N_4 will migrate toward ZnO, while the photogenerated electrons in ZnO will flow in the opposite direction. Eventually, they will recombine at the interface to form an S-type heterojunction.[48] This process effectively enhances the separation efficiency of the photogenerated charge carriers, thereby improving photocatalytic reduction efficiency. The annealed ZnO–CN was further characterized using XPS, and the results are shown in Figure 2k,l. In the N 1s spectrum, compared to pure C_3N_4, the binding energy of characteristic peaks of N—H_x, N—C_3, and C═N—C in ZnO-CN shift up by 0.18, 0.14, and 0.14 eV, respectively. In contrast, in the Zn 2p spectrum, the Zn $2p_{1/2}$ and Zn $2p_{3/2}$ peaks shift downward by 0.32 and 0.27 eV,

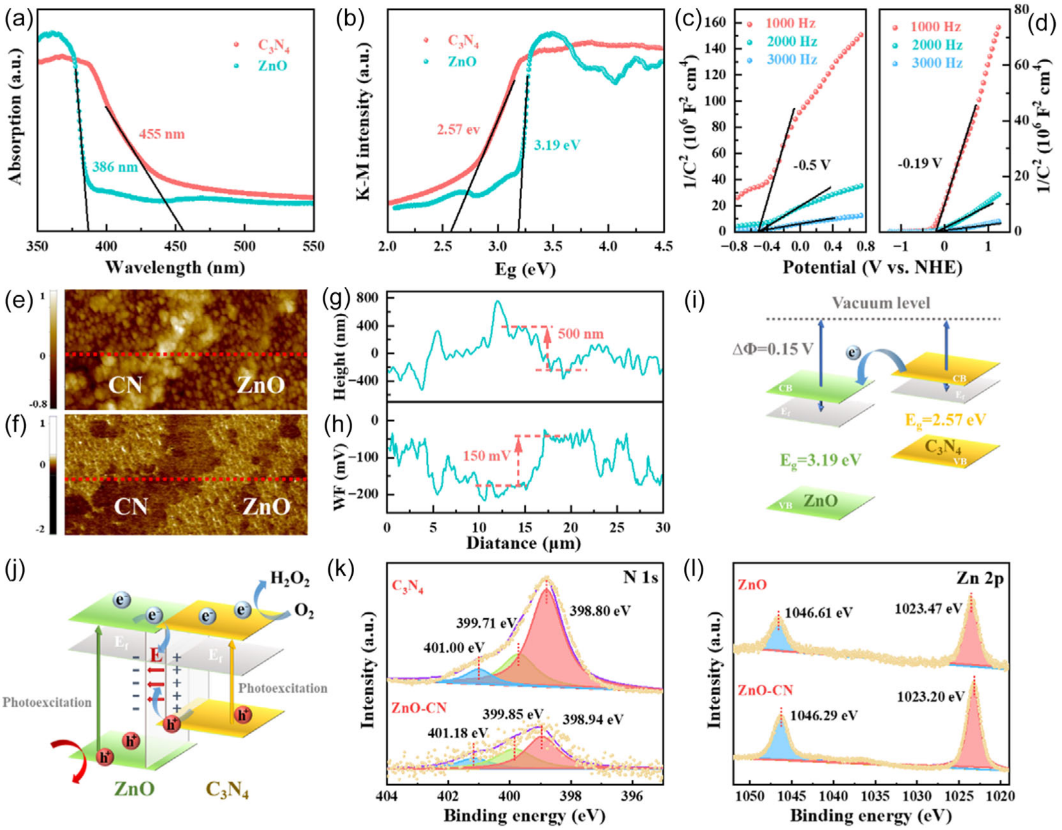

Figure 2. a) Light absorption spectra of C_3N_4 and ZnO. b) Optical bandgap diagram of C_3N_4 and ZnO. MS (Mott–Schottky) plots with frequency of 1000, 2000, and 3000 Hz of c) C_3N_4 and d) ZnO. e) AFM surface morphology and f) KPFM image of C_3N_4 and ZnO. g) Height along the red dot line in (e) and h) is the measured work function along the red dot line in (f). The band structure and the possible charge transfer in ZnO–CN i) before and j) after contact. k) XPS spectra of N 1s of C_3N_4 and ZnO–CN. l) XPS spectra of Zn 2p of ZnO and ZnO-CN.

respectively. These shifts can be attributed to the electron transfer at the interface of the heterostructure formed between C_3N_4 and ZnO.[24,29,49]

The key to improve the catalytic performance of ZnO-CN through the thermoelectric effect of ZnO is to align their thermoelectric field. As an n-type semiconductor, ZnO must have a vertical temperature gradient with high temperature at the top and low at the bottom. To increase the vertical temperature gradient in the ZnO nanoarrays through LSPR effect, Au NPs were deposited on the top of the ZnO nanoarrays through electron beam evaporation followed by rapid annealing processes. With the light shining on Au NPs, the top end of the ZnO nanoarrays are rapidly heated up due to the LSPR effect, thereby vastly enhancing the thermoelectric potential.[50,51] **Figure 3**a,b show the top-view morphology of the pure ZnO nanoarrays and the ZnO/Au film, respectively. No significant morphological changes are observed on the surface after Au deposition. As shown in Figure 3c, after annealing, Au NPs are uniformly distributed at the top of the ZnO nanoarrays. These nanoparticles are formed via the rapid melting and followed solidification by cooling of the Au film.[52] The inset shows an enlarged SEM image with an average particle size of ≈20 nm. Furthermore, the Au NPs are primarily coated at the top of the ZnO nanoarrays due to their orientation.[53] The compared XRD patterns of the composite sample with Au NPs and pure ZnO shows that the modification with Au NPs does not significantly distort the lattice of ZnO, and due to the low loading of Au, no discernible Au diffraction peaks are observed (Figure S3a, Supporting Information). The ZnO/Au was further characterized by XPS, two characteristic peaks at 86.6 and 82.8 eV correspond to Au $4f_{5/2}$ and Au $4f_{7/2}$, respectively, which confirm the successful decoration by Au NPs (Figure S3b, Supporting Information).[14] The morphology of the ZnO/Au-CN closely resembles that of ZnO-CN, with a uniform C_3N_4 catalyst layer covering the surface. The XRD pattern and the FTIR spectrum show that neither ZnO nor C_3N_4 has change its structure integrity due to the Au NPs coating (Figure S4, Supporting Information).

Infrared thermal imaging was employed to evaluate the photothermal conversion ability of C_3N_4, ZnO, ZnO-CN, ZnO/Au, and ZnO/Au-CN. A 200 mW AM 1.5 G xenon lamp was used as the light source, and the surface temperature map were recorded at 10, 20, 30, 60, 120, 180, and 240 s, as shown in Figure 3d. The results manifest the superior photothermal conversion efficiency of ZnO compared to pure C_3N_4. As indicated by the temperature curves, the surface temperature of pure C_3N_4 stabilizes at ≈32.2 °C, while the surface temperature of pure ZnO is 38.5 °C, which is 6.3 °C more than C_3N_4 (Figure S5a, Supporting Information). As shown in Figure 3e, ZnO has negligible light absorption beyond

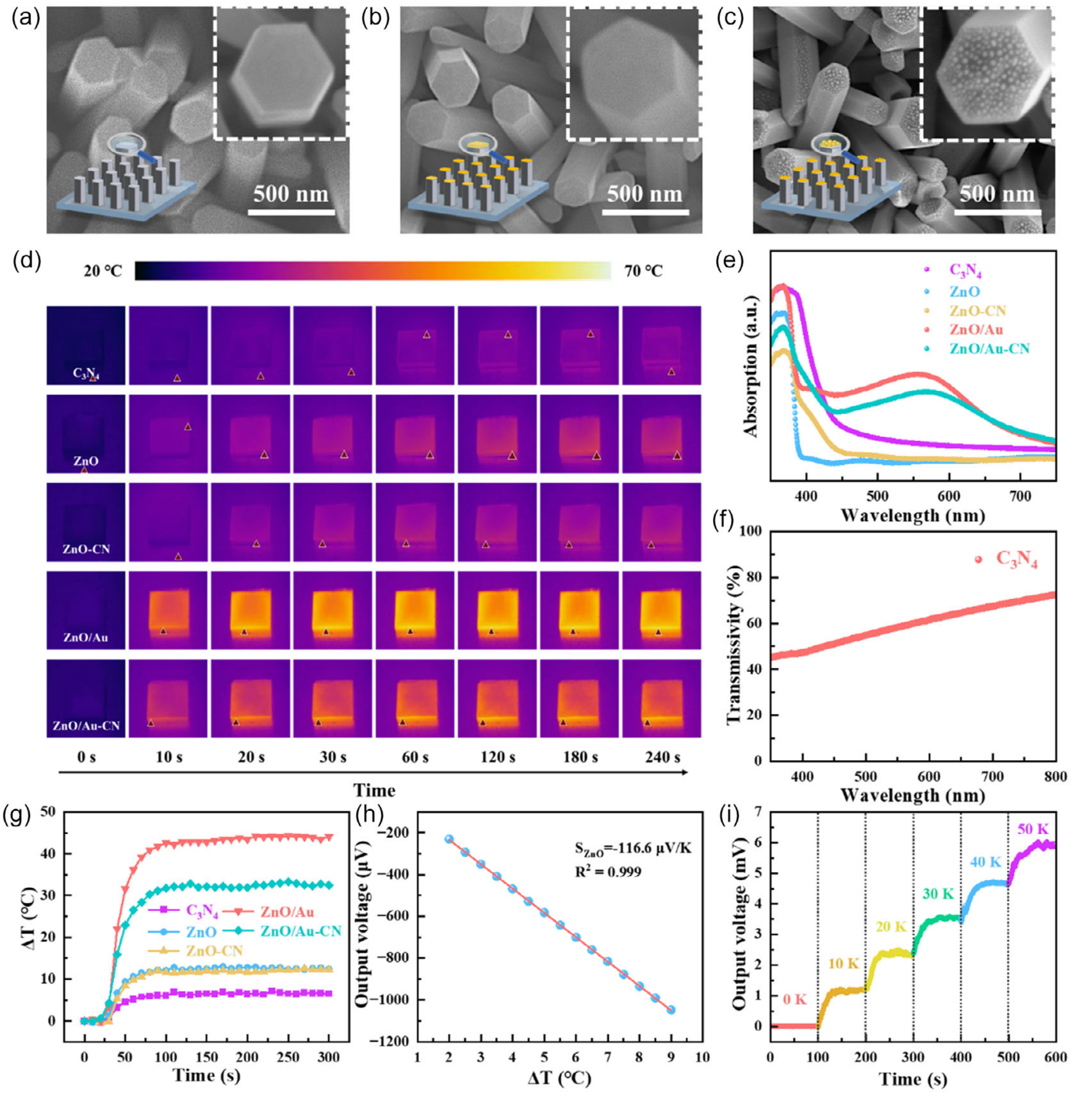

Figure 3. Top-view SEM images of a) ZnO, b) ZnO/Au film, and c) ZnO/Au NPs, the upright insets show the corresponding high-magnification SEM images. d) Infrared images of C_3N_4, ZnO, ZnO–CN, ZnO/Au, and ZnO/Au–CN under different light illumination time, the incident light is AM 1.5 G with a power of 200 mW. e) Light absorption spectra of C_3N_4, ZnO, ZnO–CN, ZnO/Au, and ZnO/Au–CN. f) Light transmission spectrum of thin C_3N_4 film. g) Vertical temperature difference test curves of C_3N_4, ZnO, ZnO–CN, ZnO/Au, and ZnO/Au–CN. h) Seebeck coefficient of ZnO nanoarrays. i) Thermoelectric output of ZnO nanoarrays with different temperature gradients.

400 nm, which suggests that the higher photothermal conversion capacity of ZnO is primarily attributed to the interwoven array structure. This structure creates high light trapping capability due to the array gaps, thereby improving light capturing efficiency.[54] Upon further modification with a thin layer of C_3N_4, the surface temperature stabilizes at around 37.6 °C, which is ≈1 °C lower than that of pure ZnO. As shown in Figure 3f, the measured light transmission spectrum of C_3N_4 thin layer with the same thickness indicates that the reduction is due to partial absorption of incident light by the C_3N_4 layer. Figure 3e demonstrates an intense absorption of ZnO/Au-CN at 550 nm, which corresponds to the LSPR characteristic light absorption of the Au NPs.[55] The LSPR effect of Au NPs increases the local temperature at the top of the ZnO nanorods, thus amplify the vertical temperature gradient in the ZnO/Au (Figure S6, Supporting information). The surface temperature of the ZnO/Au stabilizes at 70.1 °C that nearly is double of the pure ZnO. After the modification with C_3N_4, the equilibrium surface temperature of the ZnO/Au-CN is about 59.2 °C. This slight decrease compared to ZnO/Au is a result of the partial absorption of incident light by the thin C_3N_4 layer. The temperature at the cold end of the substrate under illumination shows minimal changes and almost no significant differences among all the samples (Figure S5b, Supportinf Information). Figure 3g presents the calculated vertical temperature gradient curves of different samples, demonstrating that ZnO/Au-CN has the maximum stable temperature gradient of ≈33.4 °C, which is a 2.8-fold increase compared to ZnO-CN. A home-built testing platform was used to characterize the

thermoelectric performance of the ZnO nanoarrays (Part 2 in the Supporting Information). By adjusting the input power of the Peltier cooling plate and the heating plate, a temperature gradient of 2–9 K was built up between the top and bottom electrodes of the ZnO nanoarrays. The measured output thermoelectric potential versus temperature gradient is plotted in Figure 3h. The Seebeck coefficient of the ZnO nanoarrays can be extracted from the slope of the fitted line,[56–58] which is approximately $-116.6\ \mu V\ K^{-1}$. The negative Seebeck coefficient indicates the n-type semiconductor property of ZnO that is consistent with the MS curve result shown in Figure 2d.[34,59,60] The output potential of ZnO under temperature difference of 10–50 K is shown in Figure 3i. The output potential increases steadily with the temperature gradient, and they are 1.19, 2.27, 3.52, 4.65, and 5.94 mV at temperature gradients of 10, 20, 30, 40, and 50 K, respectively. These results further highlight the thermoelectric response of the ZnO nanoarrays and their suitability for thermoelectric catalytic applications.

The photocatalytic H_2O_2 production capabilities of C_3N_4, ZnO, ZnO-CN, and ZnO/Au-CN were tested to assess their catalytic performance. To eliminate the contribution from thermoelectric properties of ZnO, a constant-temperature catalytic reaction cell was designed, as shown in **Figure 4**a. The photocatalytic H_2O_2 production rates for C_3N_4, ZnO, ZnO-CN, and ZnO/Au-CN are 11.01, 11.65, 20.56, and 23.21 $mmol\ h^{-1}\ m^{-2}$, respectively, under constant-temperature and presented in Figure 4b. The electrochemical linear sweep voltammetry (LSV) and IT curves of each sample were recorded at constant room temperature, as shown in Figure 4c,d. The photocurrent of ZnO-CN reaches 0.59 $mA\ cm^{-2}$ at a bias of 1.0 V (vs. SCE), which is significantly higher than that of C_3N_4 (0.08 $mA\ cm^{-2}$) and ZnO (0.21 $mA\ cm^{-2}$). After being modified with Au NPs, the photocurrent further increases to 0.68 $mA\ cm^{-2}$. These results demonstrate the enhancement of formed heterojunction and LSPR effect of Au NP for the catalytic efficiency of the composite. Those enhancements can be attributed to the built-in electric field at the interface, which promotes the separation of high-energy photogenerated carriers and further acceleration of the low-energy carriers recombination at the interface.[35,61] To investigate the effect of temperature gradients on photocatalytic performance, a variable-temperature reaction cell was fabricated by 3D printing, as shown in Figure 4e. The reaction cell consists of two parts: the upper section serves as the catalytic reaction chamber, while the lower section functions as a cooling chamber. The test sample is loaded between the two sections and sealed with rubber gaskets. The circulating cooling water is pumped into the lower chamber and its temperature is precisely controlled using a chiller (Figure S7, Supporting Information). It is very difficult to measure the temperature at the hot end of the sample during the catalytic reaction and considering that with the same configuration and light illumination condition, the hot end should have the same temperature. Therefore, the temperature at the cold end can be used as an indicator to reflect the temperature gradient. It means that the lower the temperature of cold end the larger temperature gradient is. Figure 4f presents H_2O_2 production efficiency by using C_3N_4, ZnO, ZnO-CN, and ZnO/Au-CN as photocatalyst under varying temperature gradients. For pure C_3N_4 and ZnO, the photocatalytic performance gradually increases as the cold end temperature rises. The H_2O_2 production rates of C_3N_4 and ZnO reach the maximum values of 11.88 and 16.83 $mmol\ h^{-1}\ m^{-2}$, respectively with a cold end temperature of 40 °C. This can be attributed to the elevated overall temperature, which activates the catalytic performance and consequently accelerates the chemical reaction rate.[62–64] However, ZnO-CN and ZnO/Au-CN exhibit a remarkable opposite trend. As the temperature of cold end decreases from 40 to 2 °C, the H_2O_2 yield rate with ZnO-CN catalyst increases from 19.51 to 27.24 $mmol\ h^{-1}\ m^{-2}$.

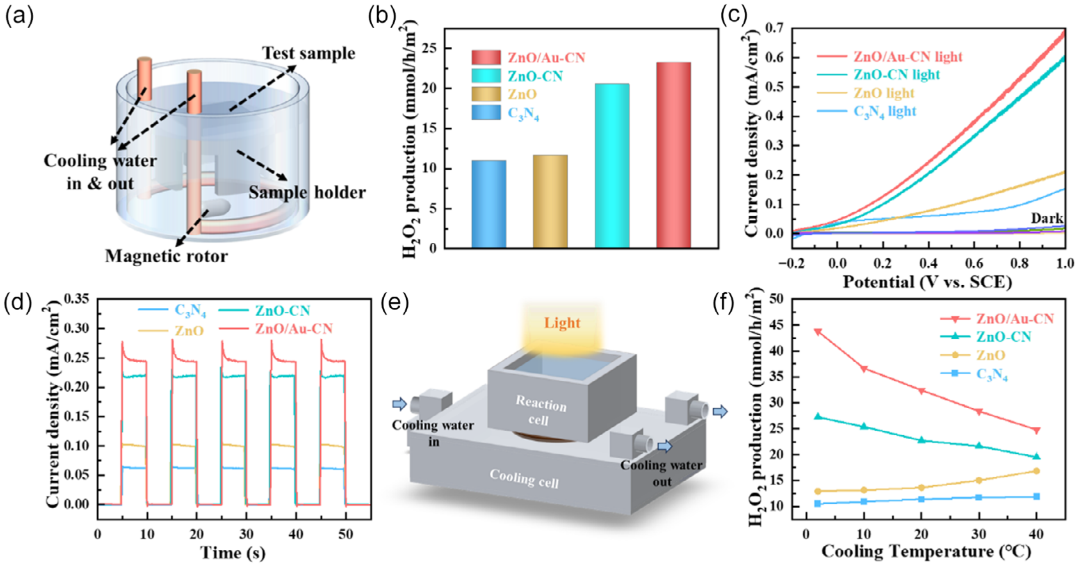

Figure 4. a) Constant-temperature photocatalytic reaction cell. The detailed description of the experimental setup can be found in Part 3 (Supporting Information). b) Photocatalytic H_2O_2 production, c) LSV and d) I–T (current–time) curves of C_3N_4, ZnO, ZnO-CN, and ZnO/Au-CN under constant room temperature. e) Variable-temperature photocatalytic reaction cell. f) Comparison of photocatalytic H_2O_2 yield performance of C_3N_4, ZnO, ZnO–CN, and ZnO/Au–CN, with the temperatures controlled by the cooling cell in the reaction.

It can be attributed to enhancement of photogenerated carriers separation in the composite materials due to the intensified built-in electric field by the thermoelectric potential caused by the increasement of vertical temperature gradient within ZnO.[65] The ZnO/Au-CN shows an even more prominent photocatalytic performance enhancement owing to its stronger photothermal conversion capability. When the temperature of the cold end is 2 °C, it achieves the highest photocatalytic performance, with a H_2O_2 production rate of 43.79 mmol h^{-1} m^{-2}. It is 4.2 times and 3.4 times higher than that of pure C_3N_4 and pure ZnO, respectively, under the same conditions. It is also 1.9 times higher than that of ZnO/Au-CN under a constant-temperature that rivals or even surpasses many ZnO powder-based catalysts. To evaluate the stability of the ZnO/Au-CN, a cyclic catalytic reaction test was performed under the circulating cooling water of 2 °C. The results indicate almost no observable change in the production rate at the same sampling points during each cycle. After six hours of continuous cyclic test, the H_2O_2 production rate of ZnO/Au-CN was 40.19 mmol h^{-1} m^{-2}, which keeps 91.1% of the first cycle (Figure S8a, Supporting Information). Additionally, C_3N_4 remained uniformly distributed on the surface of the ZnO/Au nanoarrays without observable damage or detachment (Figure S8b, Supporting Information). The XRD and FTIR spectra of ZnO/Au-CN before and after the reaction reveal no noticeable changes in the diffraction peaks of ZnO or the characteristic infrared absorption peaks of C_3N_4 (Figure S8c,d, Supporting Information). This demonstrates the excellent structural stability of ZnO/Au-CN.

To further investigate the enhancing mechanism of the ZnO thermoelectric effect on the catalytic reaction, electrochemical tests were conducted under various temperature conditions. The temperature gradient during the test was established using the same method as in the variable-temperature photocatalytic H_2O_2 production reaction (Figure S9, Supporting Information). **Figure 5**a presents the IT curves of ZnO/Au-CN under different temperature gradients. It is evident that as the cold end temperature decreases from 40 to 2 °C, the photocurrent density increases from 0.358 to 0.661 mA cm^{-2}. Similarly, the electrochemical impedance spectra (EIS) test results in Figure 5b reveal that the internal transport resistance of ZnO/Au-CN gradually decreases as the temperature gradient increases. Furthermore, 0.05 M Na_2SO_3 was used as a hole scavenger to evaluate the carrier separation efficiency of ZnO/Au-CN under different temperature gradients. It is known that the relationship between carrier

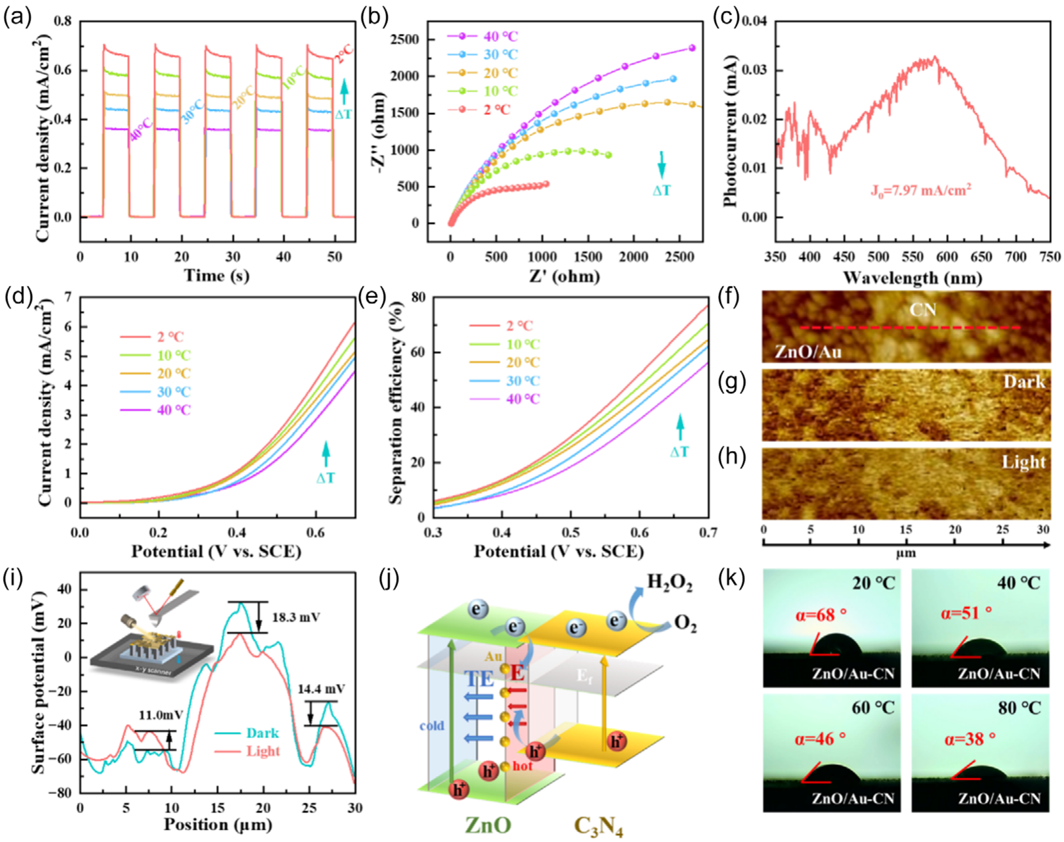

Figure 5. a) IT and b) EIS curves of ZnO/Au-CN under different cooling temperatures. c) Theoretical photocurrent of ZnO/Au-CN under the illumination of AM 1.5 G. d) LSV curves and e) carrier separation efficiency of ZnO/Au-CN with sacrificial agent under different cooling temperatures. f) Morphology of ZnO/Au-CN measured using AFM, the scanning path is shown by the red line. Surface potential distribution images under g) dark and h) light conditions. i) Surface potential curves of ZnO/Au-CN under dark and light conditions, the inset shows the diagram of surface potential test under light condition, the power of the incident light is 3 mW. j) Schematic diagram showing that how the thermoelectric effect enhances ZnO/Au-CN photocatalytic performance. k) The surface hydrophilicity measurements of ZnO/Au-CN at different temperatures.

separation efficiency and photocurrent can be described by the formula

$$J_{H_2O} = J_0 * \eta_{sep} \tag{1}$$

J_0 is obtained by integrating the AM 1.5 G standard photon flux and the absorption spectrum of ZnO/Au-CN,[14] as shown in Figure 5c. J_{H_2O} is the photocurrent density measured during the experiment, as shown in Figure 5d,e indicates that the carrier separation efficiency of ZnO/Au-CN increases progressively as the vertical temperature gradient rises. Under a bias of 0.6 V (vs. SCE), the carrier separation efficiency increases from 35.70% at 40 °C to 52.12% at 2 °C. The surface potential of ZnO/Au-CN before and after illumination was characterized by KPFM. The sample was fixed onto a Cu block with excellent thermal conductivity to maintain a stable cold-end temperature during testing (Figure S10, Supporting Information). A small amount of C_3N_4 was loaded on the top of the ZnO/Au nanoarrays, as shown in Figure 5f. It aims to expose more of the underlying thermoelectric materials to better utilize the photothermal conversion ability of ZnO/Au under illumination. The surface potential distribution of the material was scanned under both dark and bright conditions, and the results are shown in Figure 5g,h, respectively. The surface potential distribution matches well with the morphology images. The scan results along the red line are plotted in Figure 5i. After illumination, the surface potential of C_3N_4 decreases by ≈18.3 mV, while the potential on the ZnO/Au side increases by about 11.0 mV, indicating that more electrons accumulate on the C_3N_4 surface under illumination. As shown in Figure 5j, under illumination, the LSPR effect of Au NPs increases the temperature at the top of ZnO, creating a vertical temperature gradient along the ZnO nanoarrays, as indicated by the red and blue planes. As an n-type thermoelectric material, the temperature gradient drives the thermally excited electrons to migrate from the hot top to the cooler bottom, resulting in a thermoelectric field oriented from top to bottom in ZnO, as illustrated by the blue arrows. This thermoelectric field is well aligned with the built-in electric field of the ZnO/Au-CN heterojunction as marked with red arrows, which supplements the built-in electric field and significantly promote the recombination of the low-energy carriers at the interface. This synergistic effect thus effectively improves the separation efficiency of high-energy photogenerated electrons of C_3N_4 and further enhances the catalytic efficiency. Additionally, the surface hydrophilicity of ZnO/Au-CN increases progressively as the temperature rises, as shown in Figure 5k, which can be attributed to the enhanced thermal motion of both surface molecules and water molecules as the sample temperature increases.[66,67] Benefiting from the excellent photothermal conversion ability of ZnO/Au-CN, the composite becomes more conducive that improves the contact between the catalyst surface and the reactants during the liquid-phase reaction process, thereby elevating its catalytic performance.

To further investigate the mechanism of the thermoelectric field resulted catalytic performance enhancement, density functional theory (DFT) based electronic structure calculations of ZnO-CN heterojunctions were conducted, the detailed parameter settings are provided in Part 4 (Supporting Information). First, dynamically stable structures of the curved C_3N_4 monolayer and ZnO monolayer were built.[68] As shown in **Figure 6**a, the optimized crystal structure of the C_3N_4 monolayer that contains 14 atoms per unit cell with lattice constant of 3.28 Å. Figure 6b shows the crystal structure of ZnO that includes 2 atoms per unit cell with an optimized lattice parameter of 7.13 Å. Thus, a heterojunction consists of 1 C_3N_4 unit cell and 4 ZnO unit cells (a total of 22 atoms) was constructed. The stacking configuration of the heterojunction was optimized using the Van der Waals correction method. The optimized structure is shown in Figure 6c,d with an optimized lattice constant and interlayer distance of 6.77 and 2.275 Å, respectively. They are all much larger than the sum of the empirical atomic radii of Zn and N (1.35 and 0.65 Å),[69] indicating that the two materials are coupled through electrostatic Van der Waals interactions but no chemical bonds.[70] To further analyze the electronic properties of the heterojunction, we investigated their band structures as shown in Figure 6e–g. It illustrated that C_3N_4 is a semiconductor with indirect bandgap of 2.76 eV from G to K. This is in good agreement with the experimentally measured value of 2.70 eV. The corresponding density of states (DOS) plot reveals that the valence band (VB) of C_3N_4 is primarily composed of the N 2p states, while the conduction band (CB) contains contributions from both N 2p and C 2p states. ZnO exhibits a G–G bandgap of 3.06 eV that closely matches the experimentally measured value of 3.2 eV. The DOS plot indicates a strong orbital hybridization from Zn and O in ZnO with contributions in both the CB and VB. ZnO–CN has a 2.38 eV indirect G-M type bandgap. Both the conduction band minimum (CBM) and valence band maximum (VBM) are contributed by C_3N_4. An important feature of Van der Waals heterostructures is their anisotropic electronic properties perpendicular to the heterostructure, which roots from the asymmetric structure along the direction that is perpendicular to the contact interface (the z-axis). This structural asymmetry induces a built-in electric field in the heterostructure, which plays a crucial role in photocatalytic applications.

The variation of the built-in electric field within the heterojunction was analyzed through 3D differential charge density distribution under different states. The differential charge density is defined as the charge density of the heterostructure subtracts the contribution from constituent layers (ZnO and C_3N_4). The middle image inset in Figure 6h represents the charge neutral state of ZnO-CN heterojunction, where an electron depletion region forms at the ring holes of the C_3N_4 layer, while Zn atoms absorb electrons from the underlying N atoms. To better understand the distribution of electrons, and gain/loss regions along the z-axis, the differential charge density of the heterostructure along the z-axis was integrated. The formula is given as follows

$$\Delta\rho(z) = \int \rho_{ZnO-CN} dx dy - \int \rho_{ZnO} dx dy - \int \rho_{C_3N_4} dx dy \tag{2}$$

where ρ_{ZnO-CN}, ρ_{ZnO}, $\rho_{C_3N_4}$ represent the charge densities of ZnO-CN, ZnO, and C_3N_4, respectively.[70,71] It is evident from the results that electrons are depleted near C_3N_4 and accumulated at ZnO, creating a significant built-in electric field that has the direction pointing from C_3N_4 to ZnO at the interface. This built-in electric field drives photogenerated holes to migrate from C_3N_4 to ZnO and photogenerated electrons move oppositely. This prolongs the carrier lifetimes and lifts the potential

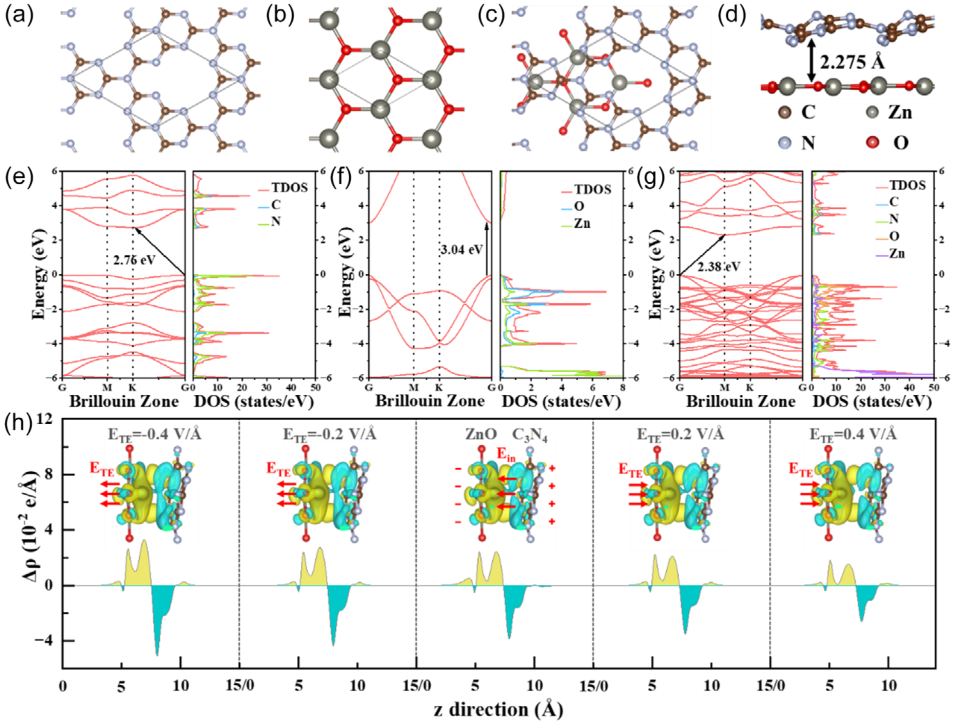

Figure 6. Structures of a) C_3N_4, b) ZnO, and c) ZnO-CN. d) Crossview of ZnO-CN. Calculated electronic band structure and density of states of e) C_3N_4, f) ZnO, and g) ZnO-CN. h) Planar-averaged electron density difference $\Delta\rho$ of ZnO-CN heterojunction, the inset images show the crossview charge density difference images of ZnO-CN with different bias voltages, where the yellow and cyan areas refer to the accumulation and depletion of electrons, respectively.

energy of the photogenerated electrons, ultimately improving the catalytic performance of the composite material. To further investigate the mechanism by which the thermoelectric field influences catalytic performance, electric fields with different relative orientations and intensities were applied along the z-axis of the heterojunction. When the electric fields are parallel to the built-in electric field in the heterojunction, there is an enhanced electron accumulation at ZnO and depletion at the C_3N_4 side, resulting in a strong built-in electric field pointing from C_3N_4 to ZnO. Furthermore, the strengthening of the built-in electric field becomes more prominent as increasing the thermoelectric field. This amplified built-in electric field further facilitates the separation of photogenerated carriers, which are consistent with the experimental results. Conversely, when the applied electric field opposes the built-in electric field, the migration of electrons from C_3N_4 to ZnO is hindered, weakening the built-in electric field and reducing the carrier separation efficiency, consequently, deteriorates the photocatalytic performance. Furthermore, the band structure of the heterojunction undergoes slight changes under the influence of the thermoelectric field. Specifically, when the external electric field aligns with the built-in electric field, the conduction band edge of the heterojunction shifts upward (Figure S11, Supporting Information). This enhances its reduction capability and therefore promotes the reduction of O_2 for H_2O_2 production.

These results indicate that coating the top of the ZnO nanoarrays with Au NPs can significantly increase the vertical temperature gradient of them under illumination. The increasement of temperature gradient further enhances thermoelectric potential output and therefore strengthens the intensity of the built-in electric field in the ZnO/Au-CN heterojunction. This further improves the spatial separation efficiency of the photogenerated electrons in C_3N_4 and the photogenerated holes in ZnO. As a result, the catalytic efficiency of the composite material is substantially enhanced.

3. Conclusion

In this work, we designed a highly aligned ZnO nanoarray that exhibits dual catalytic and thermoelectric properties. By integrating C_3N_4 nanosheets into the ZnO nanoarray, a vertical ZnO-CN thermoelectric catalytic heterojunction was fabricated. The alignment of the thermoelectric potential along the ZnO nanorods enhances the intensity of the built-in electric field within the heterojunction under illumination. Additionally, decorating Au NPs on the top of ZnO nanoarrays further elevates their thermoelectric performance compared to the bare ZnO-CN due to a 2.8-fold enhancement in temperature gradient induced by LSPR effect. Through a self-built temperature-variable photocatalytic reaction cell, the ZnO/Au-CN demonstrates a photocatalytic H_2O_2 production rate of 43.79 $\text{mmol h}^{-1}\,\text{m}^{-2}$ with 2 °C cooling water. This enhancement stems from the extent of the built-in electric field within the heterojunction, driven by thermoelectric potential, which effectively facilitates the separation of photogenerated charge carriers. Additionally, the thermoelectric field raises the conduction band of the composite material, further enhancing its photocatalytic reduction capability. This work opens an avenue in the design of high efficiency thermoelectric catalytic systems.

Supporting Information

Supporting Information is available from the Wiley Online Library or from the author.

Acknowledgements

This work was financially supported by the National Key R&D Program of China (grant no. 2022YFC3006303).

Conflict of Interest

The authors declare no conflict of interest.

Data Availability Statement

The data that support the findings of this study are available from the corresponding author upon reasonable request.

Keywords

Au localized surface plasmon resonance effect, built-in electric field, photocatalytic H_2O_2 production, thermoelectric catalytic heterojunctions

Received: March 31, 2025
Revised: May 28, 2025
Published online:

---

[1] Y. Sun, L. Han, P. Strasser, *Chem. Soc. Rev.* **2020**, *49*, 6605.
[2] H. Hou, X. Zeng, X. Zhang, *Angew. Chem. Int. Ed.* **2020**, *59*, 17356.
[3] Z. Chen, D. Yao, C. Chu, S. Mao, *Chem. Eng. J.* **2023**, *451*, 138489.
[4] S. Wu, X. Wang, H. Yu, *Chin. J. Struct. Chem.* **2024**, *43*, 100457.
[5] J. M. Campos-Martin, G. Blanco-Brieva, J. L. Fierro, *Angew. Chem. Int. Ed.* **2006**, *45*, 6962.
[6] Y. Zhao, P. Zhang, Z. Yang, L. Li, J. Gao, S. Chen, T. Xie, C. Diao, S. Xi, B. Xiao, *Nat. Commun.* **2021**, *12*, 3701.
[7] T. Liu, Z. Pan, J. J. M. Vequizo, K. Kato, B. Wu, A. Yamakata, K. Katayama, B. Chen, C. Chu, K. Domen, *Nat. Commun.* **2022**, *13*, 1034.
[8] X. Zhang, D. Gao, B. Zhu, B. Cheng, J. Yu, H. Yu, *Nat. Commun.* **2024**, *15*, 3212.
[9] X. Yin, H. Shi, Y. Wang, X. Wang, P. Wang, H. Yu, *Acta Phys.-Chim. Sin.* **2024**, *40*, 2312007.
[10] C. Bie, B. Cheng, J. Fan, W. Ho, J. Yu, *EnergyChem* **2021**, *3*, 100051.
[11] Y. Xia, B. Zhu, X. Qin, W. Ho, J. Yu, *Chem. Eng. J.* **2023**, *467*, 143528.
[12] L. Zhang, J. Zhang, H. Yu, J. Yu, *Adv. Mater.* **2022**, *34*, 2107668.
[13] X. Zhao, Y. You, S. Huang, Y. Wu, Y. Ma, G. Zhang, Z. Zhang, *Appl. Catal. B* **2020**, *278*, 119251.
[14] R. Sun, X. Jiang, M. Zhang, Y. Ma, X. Jiang, Z. Liu, Y. Wang, J. Yang, M. Xie, W. Han, *J. Catal.* **2019**, *378*, 192.
[15] Y. Guo, W. Shi, Y. Zhu, *EcoMat* **2019**, *1*, 20.
[16] T. Han, X. Cao, K. Sun, Q. Peng, C. Ye, A. Huang, W. Cheong, Z. Chen, R. Lin, D. Zhao, *Nat. Commun.* **2021**, *12*, 4952.
[17] X. Chen, J. Wang, Y. Chai, Z. Zhang, Y. Zhu, *Adv.Mater* **2021**, *33*, 2007479.
[18] J. Li, L. Cai, J. Shang, Y. Yu, L. Zhang, *Adv. Mater.* **2016**, *28*, 4059.
[19] J. Low, J. Yu, M. Jaroniec, S. Wageh, A. Al-Ghamdi, *Adv. mate.* **2017**, *29*, 1601694.
[20] H. Yang, *Mater. Res. Bull.* **2021**, *142*, 111406.
[21] X. Li, L. Zhao, J. Yu, X. Liu, X. Zhang, H. Liu, W. Zhou, *Nano-Micro Lett.* **2020**, *12*, 1.
[22] Y. Xu, Z. Zhou, M. Zou, Y. Liu, Y. Zheng, Y. Yang, S. Lan, J. Lan, C. Nan, Y. Lin, *Mater. Today* **2022**, *54*, 225.
[23] M. Sun, B. Liu, W. Han, Z. Zhang, M. Xie, *Appl. Catal. B* **2022**, *304*, 120980.
[24] P. He, L. Zhang, L. Wu, S. Xiao, X. Ren, R. He, X. Yang, R. Liu, T. Duan, *Appl. Catal. B* **2023**, *322*, 122087.
[25] Y. Lu, H. Zhang, D. Fan, Z. Chen, X. Yang, *J. Hazard. Mater.* **2022**, *423*, 127128.
[26] R. Mulla, C. W. Dunnill, *ChemSusChem* **2019**, *12*, 3882.
[27] Y. Zhang, S. Li, J. Zhang, L. Zhao, Y. Lin, W. Liu, F. Rosei, *Natl. Sci. Rev.* **2024**, *11*, nwae036.
[28] T. Ohta, S. Asakura, M. Yamaguchi, N. Kamiya, N. Gotgh, T. Otagawa, *Int. J. Hydrogen Energy* **1976**, *1*, 113.
[29] H. Dong, L. Tong, P. Zhang, D. Zhu, J. Jiang, C. Li, *J. Mater. Sci. Technol.* **2024**, *179*, 251.
[30] Y. Xu, J. Han, Y. Luo, Y. Liu, J. Ding, Z. Zhou, C. Liu, M. Zou, J. Lan, C. Nan, *Adv. Funct. Mater.* **2021**, *31*, 2105001.
[31] Y. Dou, F. Wu, L. Fang, G. Liu, C. Mao, K. Wan, M. Zhou, *J. Power Sources* **2016**, *307*, 181.
[32] Y. Lin, I. Khan, S. Saha, C. C. Wu, S. R. Barman, F. Kao, Z. Lin, *Nat. Commun.* **2021**, *12*, 180.
[33] S. Wang, Y. Qiao, X. Liu, S. Zhu, Y. Zheng, H. Jiang, Y. Zhang, J. Shen, Z. Li, Y. Liang, *Adv. Funct. Mater.* **2023**, *33*, 2210098.
[34] K. Zhang, B. Ouyang, Y. Wang, Y. Xia, Y. Yang, *J. Materiomics* **2019**, *2*, 7647.
[35] X. Li, H. Jiang, C. Ma, Z. Zhu, X. Song, H. Wang, P. Huo, X. Li, *Appl. Catal. B* **2021**, *283*, 119638.
[36] L. Pei, H. Zhao, W. Tan, H. Yu, Y. Chen, Q. Zhang, *Mater. Charact.* **2009**, *60*, 1063.
[37] G. Liu, X. Yu, R. Xu, X. Zhu, Y. Ma, L. Ma, *Chem. Eur. J.* **2021**, *27*, 17620.
[38] F. Su, C. Xu, Y. Yu, W. Zhang, *ChemCatChem* **2016**, *8*, 3527.
[39] X. Wu, X. Wang, F. Wang, H. Yu, *Appl. Catal. B* **2019**, *247*, 70.
[40] J. Jin, Q. Liang, C. Ding, Z. Li, S. Xu, *J. Alloys Compd.* **2017**, *691*, 763.
[41] Z. Xing, Y. Chen, C. Liu, J. Yang, J. Xu, Y. Situ, H. Huang, *J. Alloys Compd.* **2017**, *708*, 853.
[42] X. Yu, C. Hu, D. Hao, G. Liu, R. Xu, X. Zhu, X. Yu, Y. Ma, L. Ma, *Solar RRL* **2021**, *5*, 2000827.
[43] G. Zhou, J. Chen, L. Wen, J. Liu, *Catal. Lett.* **2024**, *154*, 2057.
[44] Y. Ma, X. Jiang, R. Sun, J. Yang, X. Jiang, Z. Liu, M. Xie, E. Xie, W. Han, *Chem. Eng. J.* **2020**, *382*, 123020.
[45] R. Beranek, *Adv. Phy. Chem.* **2012**, *2011*, 1.
[46] D. Ramírez-Ortega, A. M. Meléndez, P. Acevedo-Peña, I. González, R. Arroyo, *Electrochim. Acta* **2014**, *140*, 541.
[47] Y. Yang, J. Liu, M. Gu, B. Cheng, L. Wang, J. Yu, *Appl. Catal. B: Environ. Energy* **2023**, *333*, 122780.
[48] Q. Xu, L. Zhang, B. Cheng, J. Fan, J. Yu, *Chem* **2020**, *6*, 1543.
[49] P. Zhang, Y. Li, Y. Zhang, R. Hou, X. Zhang, C. Xue, S. Wang, B. Zhu, N. Li, G. Shao, *Small Methods* **2020**, *4*, 2000214.
[50] D. Wu, K. Yan, Y. Zhou, H. Wang, L. Lin, H. Peng, Z. Liu, *J. Am. Chem. Soc.* **2013**, *135*, 10926.
[51] L. Zhou, Y. Tan, D. Ji, B. Zhu, P. Zhang, J. Xu, Q. Gan, Z. Yu, J. Zhu, *Sci. Adv.* **2016**, *2*, 1501227.

[52] M. Bechelany, X. Maeder, J. Riesterer, J. Hankache, D. Lerose, S. Christiansen, J. Michler, L. Philippe, *Cryst. Growth Des.* **2010**, *10*, 587.

[53] C. Zou, Y. Rao, A. Alyamani, W. Chu, M. Chen, D. A. Patterson, E. A. Emanuelsson, W. Gao, *Langmuir* **2010**, *26*, 11615.

[54] J. Zhu, Z. Yu, G. F. Burkhard, C. M. Hsu, S. T. Connor, Y. Xu, Q. Wang, M. McGehee, S. Fan, Y. Cui, *Nano lett.* **2009**, *9*, 279.

[55] D. E. Mustafa, T. Yang, Z. Xuan, S. Chen, H. Tu, A. Zhang, *Plasmonics* **2010**, *5*, 221.

[56] Y. Ren, R. Sun, X. Yu, R. Wang, W. Zhang, X. Zhu, Y. Ma, L. Ma, *Mater. Adv.* **2023**, *4*, 4455.

[57] R. Sun, R. Guo, X. Yu, Y. Ren, R. Wang, P. Zou, Z. Chen, R. Xu, Y. Ma, L. Ma, *ACS Appl. Mater. Interfaces* **2024**, *16*, 45307.

[58] R. Wang, R. Sun, Y. Ren, Y. Ma, L. Ma, *J. Mater. Sci. Mater. Eng.* **2025**, *20*, 1.

[59] X. Du, W. Tian, Z. Zhang, B. Hui, J. Pan, J. Sun, K. Zhang, *J. Materiomics* **2022**, *8*, 693.

[60] S. D. Luu, T. A. Duong, T. B. Phan, *Adv. Nat. Sci.: Nanosci Nanotechnol.* **2019**, *10*, 023001.

[61] Q. Li, Z. Guan, D. Wu, X. Zhao, S. Bao, B. Tian, J. Zhang, *ACS Sustainable Chem. Eng.* **2017**, *5*, 6958.

[62] J. F. Wu, C. H. Hung, C. S. Yuan, *J. Photochem. Photobiol. A* **2005**, *170*, 299.

[63] N. A. Barakat, M. A. Kanjwal, I. S. Chronakis, H. Y. Kim, *J. Mol. Catal. A: Chem.* **2013**, *366*, 333.

[64] Y. W. Chen, Y. H. Hsu, *Catalysts* **2021**, *11*, 966.

[65] B. Tan, M. Sun, B. Liu, X. Jiang, Q. Feng, E. Xie, P. Xi, Z. Zhang, *Nano Energy* **2023**, *107*, 108138.

[66] J. Song, L. Fan, *J. Colloid Interface Sci.* **2022**, *605*, 163.

[67] J. Drelich, E. Chibowski, D. D. Meng, K. Terpilowski, *Soft Matter.* **2011**, *7*, 9804.

[68] M. Topsakal, S. Cahangirov, E. Bekaroglu, S. Ciraci, *Phys. Rev. B* **2009**, *80*, 235119.

[69] J. C. Slater, *J. Chem. Phys.* **1964**, *41*, 3199.

[70] K. Rahimi, A. Z. Moshfegh, *Phys. Chem. Chem. Phys.* **2021**, *23*, 20675.

[71] C. Khamdang, S. Singsen, A. Ngoipala, I. Fongkaew, A. Junkaew, S. Suthirakun, *ACS Appl. Energy Mater.* **2022**, *5*, 13997.